Top-down inflation and deflation at the summit of Kīlauea Volcano, Hawai'i observed with InSAR

Scott Baker[1] and Falk Amelung[1]

Received 23 December 2011; revised 14 October 2012; accepted 23 October 2012; published 15 December 2012.

[1] We use interferometric synthetic aperture radar (InSAR) to study deformation of the summit caldera at Kīlauea Volcano during 2000–2008, which spanned both an east rift zone eruptive event in 2007 and the start of the ongoing summit eruption in 2008. The data set consists of small baseline subset (SBAS) time series generated from 270 acquisitions on three separate beam modes from the Radarsat-1 satellite. We identify 12 time periods with distinct patterns of displacement that we attribute until late 2003 to secular tectonic-driven deformation and from 2004 to 2008 to four different sources in the summit area. We model the shallow magmatic system as a spherical reservoir at 1.9 ± 0.1 km depth below the surface to the northeast of Halemaumau (source 1) and three vertically stacked sills at greater depths in the southern caldera area (source 2 at the southern edge of the caldera at 2.9 ± 0.2 km depth, source 3 to the south-southeast of the caldera at 3.4 ± 0.5 km depth, and source 4 south of the caldera at 3.6 ± 0.4 km depth). The sequence for filling of and withdrawal from these reservoirs reveals a top-down process, with sequences of both inflation and deflation initiating in the shallowest source. Inflation of source 3 is coincident with elevated seismic activity in the upper east rift zone in February 2006 and May 2007. Source 4 is elongated toward the southwest rift zone and also shows elevated seismicity that extends toward the southwest rift zone.

Citation: Baker, S., and F. Amelung (2012), Top-down inflation and deflation at the summit of Kīlauea Volcano, Hawai'i observed with InSAR, *J. Geophys. Res.*, *117*, B12406, doi:10.1029/2011JB009123.

1. Introduction

[2] Kīlauea Volcano on the Island of Hawai'i is one of the most active volcanoes in the world, providing a natural laboratory to study processes of basaltic magmatism. Since 1983, Kīlauea has been continuously erupting predominately from the Pu'u 'Ō'o vent on the east rift zone (Figure 1) [*Heliker et al.*, 2003]. Recent explosive activity began at the summit in March 2008 with the opening of a vent in Halemaumau Crater [*Wilson et al.*, 2008]. The magmatic system at the summit of Kīlauea is not a simple magma chamber geometry, but rather it consists of a complex series of dikes and sills [*Fiske and Kinoshita*, 1969; *Dawson et al.*, 2004]. Within the last 15 years, the establishment of a dense global positioning system (GPS) network and acquisitions of satellite synthetic aperture radar (SAR) data sets provide a way to measure surface displacement on the volcano.

[3] Previous geodetic studies investigated centers of inflation and deflation in and around the summit caldera using leveling, tilt, trilateration, GPS, and interferometric synthetic aperture radar (InSAR) [*Cervelli and Miklius*, 2003; *Dvorak et al.*, 1983; *Fiske and Kinoshita*, 1969; *Johnson*, 1992; *Lockwood et al.*, 1999; *Poland et al.*, 2009]. *Fiske and Kinoshita* [1969] showed multiple centers of inflation inside and to the south of the summit caldera. Nearly 2.3 m of subsidence has occurred near Halemaumau since 1975 [*Johnson et al.*, 2010], and at the same time the summit has been affected by volcanic spreading [*Delaney et al.*, 1998]. Repeated dike intrusions occur within the rift zones and affect activity of the shallow system (e.g., subsidence near Halemaumau during east rift zone dike intrusions and eruptions in 1997 [*Owen et al.*, 2000] and 2007 [*Poland et al.*, 2009; *Montgomery-Brown et al.*, 2010]).

[4] Understanding the shallow system is important because measurements of the ground deformation (e.g., inflation at a particular location) could be used as an indicator for impending eruptive activity, either at the summit or along the rift zones. The summit of Kīlauea, which is visited daily by thousands of tourists, experienced explosive eruptions in the past (in 1924, and during a 300 year period since the formation of the caldera in ~1500 [*Swanson et al.*, 2012]), so characterizing the observed deformation and resulting activity is vital for understanding the behavior of the volcano. The knowledge that is gained can be applied at other basaltic volcanic systems such as the neighboring Mauna Loa which had an intrusive period during 2002–2009 [*Amelung et al.*, 2007] or the Galapagos volcanoes which have equally or even more dynamic shallow volcanic systems [*Amelung et al.*, 2000; *Chadwick et al.*, 2006].

[1]Rosenstiel School of Marine and Atmospheric Science, University of Miami, Miami, Florida, USA.

Corresponding author: S. Baker, Rosenstiel School of Marine and Atmospheric Science University of Miami, 4600 Rickenbacker Cswy., Miami, FL 33149 USA. (sbaker@rsmas.miami.edu)

0148-0227/12/2011JB009123

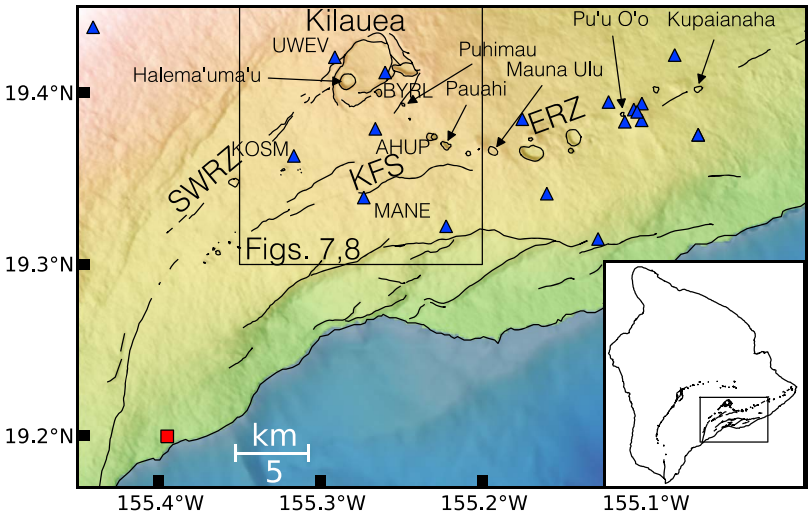

Figure 1. Map of Kīlauea's summit and rift zones showing topography and locations of main features. Blue triangles mark the locations of continuous GPS stations operated by HVO. The smaller box around the summit outlines the area covered by Figures 7 and 8. Abbreviations are as follows: ERZ, east rift zone; SWRZ, southwest rift zone; KFS, Koae Fault System. The red square indicates the reference point location for the InSAR time series.

[5] A new episode of inflation at Kīlauea's summit started in 2003 [*Poland et al.*, 2012], and, as shown below, reversed a secular subsidence trend that was dominant since the start of the Pu'u 'Ō'o eruption in 1983 [*Johnson et al.*, 2010]. The Canadian Radarsat-1 satellite acquired an excellent set of SAR imagery from 1998 to 2008. The frequently repeated acquisitions provide an opportunity to study the dynamics of magma accumulation and migration at unprecedented spatial and temporal resolution. We characterize the surface displacements from 2000 to 2008 using InSAR time series analysis and GPS measurements and infer sources of deformation in the shallow system beneath the summit, providing parameters for location and source geometry. We discuss implications for top-down inflation and deflation of magma bodies and compare our results with historic periods of activity and previous geodetic studies.

2. Data

[6] We use InSAR and GPS data to analyze the deformation at the summit of Kīlauea Volcano from January 2000 to March 2008. The two data sets are complimentary because they measure the same surface displacement. The continuous GPS data are used to support the InSAR time series analysis by providing a means to verify the accuracy of the results.

2.1. InSAR

[7] Interferograms are made using data acquired by the Canadian Space Agency's Radarsat-1 SAR satellite. At Kīlauea, Radarsat-1 data have the longest continuous time span (over 10 years), and with the 24 day repeat pass of the satellite, it is the most frequently acquired SAR data up to 2008. The primary data set consists of two beams, one ascending pass (standard beam S3, incidence angle 34–40 degrees, 86 scenes, 22 January 2000 to 16 March 2008) and one descending pass (standard beam S1, incidence angle 24–31 degrees, 96 scenes, 21 February 1999 to 17 March 2008), referred to as ascending S3 and descending S1, respectively. Due to some missed acquisitions of the ascending pass during critical time periods, a third beam completes the coverage (standard beam S6, incidence angle 45–49 degrees, 88 scenes, 31 March 1998 to 2 March 2008, used for the ascending S3 missed acquisition on 2 June 2007), referred to as ascending S6. We use the ROI_PAC SAR processing software developed at NASA's Jet Propulsion Laboratory (JPL) [*Rosen et al.*, 2004] to produce the interferograms.

[8] We use the small baseline subset (SBAS) method for generating the InSAR time series [*Berardino et al.*, 2002; *Lanari et al.*, 2004; *Gourmelen et al.*, 2010]. The SBAS method inverts a large number (in this case hundreds) of InSAR images, relying on the redundancy of multiple InSAR images to determine the surface displacement for each pixel through time. Interferometric pair selection is performed using a Delaunay triangulation in the perpendicular baseline–temporal baseline space to create an interconnected network of interferograms. We present here the network for the descending S1 data set (Figure 2). The temporal baseline values are scaled by a ratio of the perpendicular baseline threshold (600 m) to the temporal baseline threshold (10 years) following *Pepe and Lanari* [2006]. Those pairs that exceed the spatial and temporal baseline thresholds and lack sufficient Doppler overlap are removed from the network (Figure 2, dashed black lines). There is an unconnected subset due to large baselines, but this subset overlaps the larger network in time. SBAS employs the singular value decomposition (SVD) method, which allows these two separate networks to be linked. The interconnected network of interferograms allows calculation of displacement between any two acquisitions, regardless of the possibility of generating a particular interferogram. The same network procedure is applied to the other acquisition modes. In total, we calculate a network of 262 interferograms for descending S1, 262 interferograms for ascending S3, and

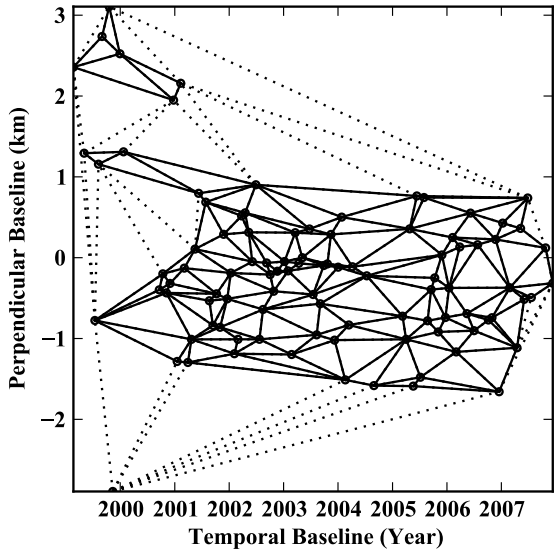

Figure 2. Triangulated network of interferometric pairs. Solid lines show candidate pairs for SBAS time series generation and dotted lines are pairs that do not meet the selection criteria (less than 600 m perpendicular baseline separation and 15% Doppler overlap).

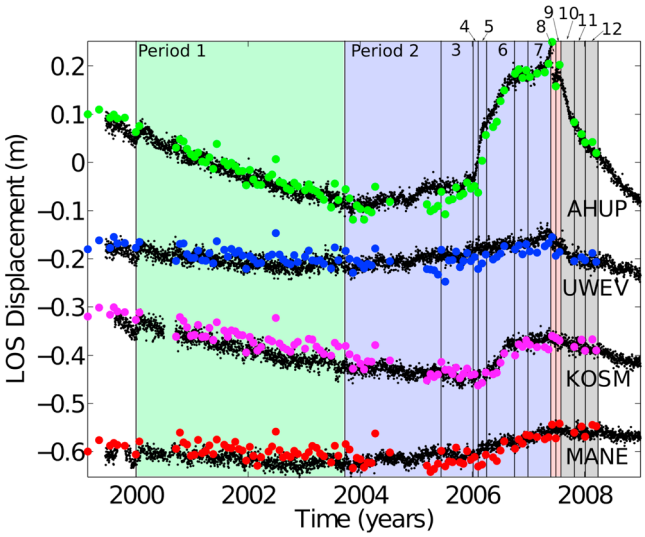

Figure 4. Colocated InSAR (colored circles, Radarsat-1 descending S1) and GPS (black dots, displacements projected into descending S1 LOS) time series around the summit of Kīlauea. Colored areas correspond to the four deformation episodes and vertical black lines separate the individual time periods identified in Table 1.

255 interferograms for ascending S6 for the time series processing. Pixels with high correlation will have phase values with lower errors, which helps to lessen the effects of phase noise and errors incurred during interferogram processing. We only use pixels with 70 percent of the interferograms having a correlation of 0.3 or higher. The time series are referenced to a single pixel that exhibits high coherence. This pixel is located far enough from the summit and rift zones to not be influenced by the deformation taking place there (Figure 1, red square). If the reference point has significant displacement, then we would not expect good agreement between the InSAR and GPS time series around the summit (Figures 3 and 4, described below). We do not apply an atmospheric correction to the time series, and given the spatial and temporal variability of this signal, it is possible that atmosphere artifacts are present at the reference point and could influence the time series at other locations. Since there is agreement between the InSAR and GPS time series, we are confident that atmospheric artifacts are not an issue.

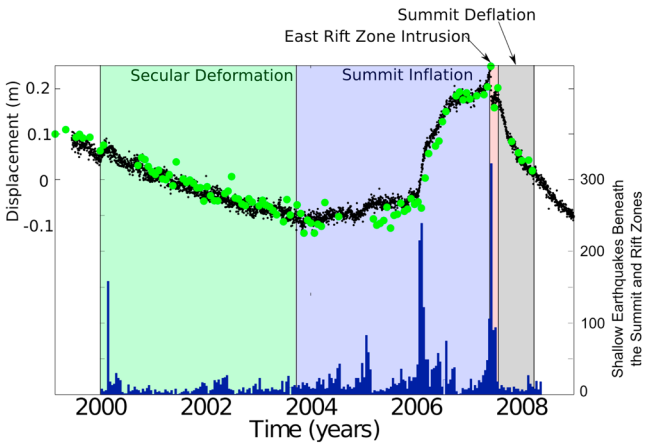

Figure 3. Colocated InSAR (green circles, Radarsat-1 descending S1) and GPS (black dots, displacements projected into descending S1 LOS) time series displacements at station AHUP. At the bottom is a histogram of shallow earthquakes (<5 km) with magnitude greater than 0.6 that occurred in the upper rift zones and summit area of Kīlauea every 2 weeks.

2.2. GPS

[9] The Hawaiian Volcano Observatory (HVO), in collaboration with Stanford University and the University of Hawai‘i, has established and maintains a dense network of continuous GPS stations on Kīlauea (Figure 1). A total of 18 stations exist with data available during the time period covered by the InSAR data. The GPS data are available for download from the University NAVSTAR Consortium (UNAVCO). GPS data were processed at the University of Miami Geodesy Lab using GIPSY-OASIS software from JPL [*Stephen et al.*, 1996]. The results provide daily point position measurements for the north-south, east-west, and vertical components in the ITRF2000 reference frame. Ocean loading is taken into account during the processing, as well as solutions for the ionosphere and troposphere. To compare GPS and InSAR results, we removed the NUVEL 1-A plate motion [*DeMets et al.*, 1994] from the GPS time series to account for the difference between an absolute (GPS) and a relative (InSAR) reference frame. The result is the Pacific plate reference frame, which can also be viewed as a reference frame local to Hawai‘i. For further comparison of the GPS and InSAR time series, we project the 3 components of the GPS data into the radar line of sight (LOS) for Radarsat-1 descending beam S1, showing that the measured motion is consistent for both data sets. The GPS station showing the largest amount of displacement in the summit area is AHUP, and Figure 3 shows the LOS projected GPS time series and the descending S1 InSAR time series at that location. The

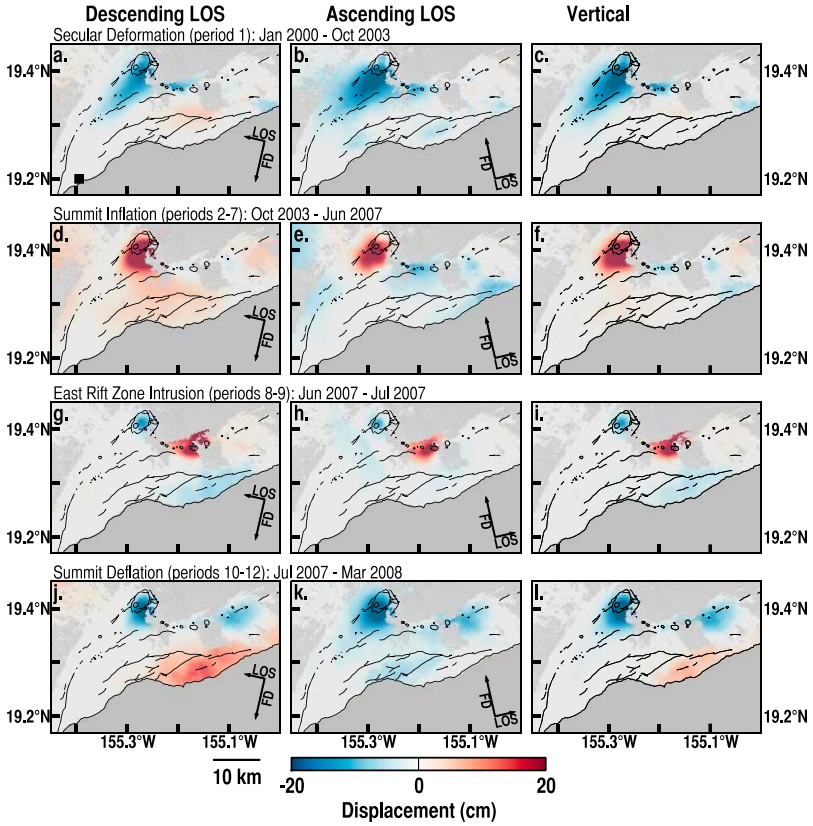

Figure 5. InSAR time series displacement maps for Radarsat-1 descending S1 LOS (left column) and ascending S3 LOS (middle column) satellite passes and the computed verticals (right column) during four episodes of deformation. Blue colors indicate motion away from the satellite for LOS and down for vertical, and red colors indicate motion toward the satellite or up. (a) Descending, (b) ascending, and (c) vertical from January 2000 to October 2003; (d) descending, (e) ascending, and (f) vertical from October 2003 to June 2007; (g) descending, (h) ascending, and (i) vertical from June 2007 to July 2007; and (j) descending, (k) ascending, and (l) vertical from July 2007 to March 2008. The dark gray areas have no data due to low coherence in the interferograms. Arrows in lower right corners show the flight direction (FD) and line of sight (LOS) of the radar. The black square in Figure 5a indicates the reference pixel location for the InSAR time series.

continuous GPS stations around the summit that are operational during the time span of the InSAR time series are shown in Figure 4 with colocated InSAR time series. In both figures, the GPS and InSAR time series show similar results between these independent data sets.

3. Surface Displacement Activity at Kīlauea's Summit

[10] Based on the time-variable pattern of seismicity and surface displacement (discussed below), we categorize the activity at Kīlauea's summit between 2000 and 2008 into four episodes of deformation. We define these episodes as secular deformation from January 2000 to October 2003, summit inflation from October 2003 to June 2007, east rift zone intrusion and eruption from June 2007 to July 2007, and summit deflation from July 2007 to March 2008. Figure 5 shows the descending and ascending LOS displacements (left and middle columns, respectively) for these periods as well as the computed vertical motion (right column). Red colors indicate up (or toward the satellite for LOS displacements) and blue indicates down (or away from the satellite). Temporal changes in the surface displacement pattern are clearly represented in the vertical component of the displacement field which we calculate using the ascending and descending LOS displacements [*Wright et al.*, 2004]. Using the SBAS time series displacements from different look angles on ascending and descending passes of the satellite, we can compute the three components of motion (north, east, and vertical). The northern component contains the most error and is poorly resolved because the satellite has approximately a 12 degree angle from north, so the radar is most sensitive to the vertical and east-west directions. Given that inflation and deflation of magmatic sources will produce a predominately vertical component of motion located directly above the source, we will now focus on the vertical measurements calculated from the InSAR time series. This provides a better location for the source of deformation compared to the other two components.

[11] The secular deformation episode shows a broad area of subsidence around the summit and within the rift zones, with the maximum subsidence of 20 cm located just to the south of the summit caldera (Figure 5c). The summit inflation episode shows a broad area of inflation around the

Table 1. Time Periods of Deformation at the Summit of Kīlauea and Active Sources of Deformation[a]

Period	Dates	Time (Days)	Active Source	Vertical Displacement (cm)
	Secular Deformation			
1	22 Jan 2000 to 28 Sep 2003	1345		−23
	Summit Inflation			
2	28 Sep 2003 to 31 Jul 2005	672	1	6
3	31 Jul 2005 to 15 Jan 2006	168	2	3
4	15 Jan 2006 to 8 Feb 2006	24	1	4
5	8 Feb 2006 to 28 Mar 2006	48	3	11
6	28 Mar 2006 to 6 Oct 2006	192	4	14
7	27 Feb 2007 to 3 Jun 2007	96	3	5
	East Rift Zone Intrusion			
8	3 Jun 2007 to 27 Jun 2007	24	1	−16
9	27 Jun 2007 to 21 Jul 2007	24	1	6
	Summit Deflation			
10	20 Jul 2007 to 25 Oct 2007	96	2	−15
11	24 Oct 2007 to 5 Jan 2008	72	3	−6
12	5 Jan 2008 to 17 Mar 2008	72		−4

[a]The time period bounds are based on SAR acquisition times and may be off by up to 24 days given the repeat-pass interval of the satellite. Maximum vertical displacement for each time period is given and locations of the sources and maximum displacement are best seen in Figure 8.

summit with a maximum vertical displacement of 34 cm and continued subsidence within the east rift zone (Figure 5f). The 2007 east rift zone intrusion and eruption episode initiates deflation at the summit with a maximum subsidence of 16 cm within the caldera and 30 cm of uplift in the east rift zone at the site of the eruption (Figure 5i). The summit deflation episode shows a broad area of subsidence around the summit with a maximum of 27 cm, subsidence around Pu‘u ‘Ō‘o with a maximum of 14 cm (Figure 5l). In contrast to the summit inflation and secular deformation episodes, there is evidence for uplift on the south flank along the coast (Figure 5l).

[12] Changes in the GPS and InSAR time series and changes in earthquake activity (Figures 3 and 4) revealed more details about the activity occurring during the four episodes described above. We defined 12 separate time periods (Table 1) that characterize the changes in displacement around Kīlauea's summit from January 2000 to March 2008. The time period bounds are based on SAR acquisition times and may be off by up to 24 days given the repeat-pass interval of the satellite. The secular deformation episode is detailed by a single period (referred to as period 1) and spans the longest amount of time at 4 years. Following period 1, the summit inflation episode is divided into 6 periods (period 2 through period 7) and spans the next 3 years. The east rift zone intrusion and eruption episode is detailed by two periods, periods 8 and 9, with each covering a 24 day period in June and July 2007. The summit deflation episode is divided into 3 periods (period 10 through period 12), and covers up to March 2008, when Radarsat-1 acquisitions cease. In the following, we zoom into the summit area and describe details of the displacement pattern and how it changes through time.

3.1. Secular Deformation: Period 1

[13] The first period, from 22 January 2000 to 28 September 2003, is characterized by a broad area of subsidence around the summit and upper rift zones (Figure 6a). As discussed above, a maximum subsidence of 23 cm is located just to the south of the caldera. The rate and amount of subsidence decreases further down the rifts and away from the summit. The GPS stations around the summit and rift zones (AHUP, KOSM, MANE, and UWEV) show southeast motion increasing toward the south (Figure 6a).

3.2. Summit Inflation: Periods 2 Through 7

[14] The summit inflation episode leading up to the 2007 intrusion and eruption is covered by six time periods (periods 2–6, Figures 6b–6g). The location of the inflation shifts between the inner caldera and an area on the southeastern edge of the caldera during three time periods, period 2 (Figure 6b), period 3 (Figure 6c), and period 4 (Figure 6d). Inflation during period 2 is centered inside the caldera to the northeast of Halemaumau Crater with a maximum displacement of 6 cm (Figure 6b). During period 3, the center of inflation shifted to the southeastern edge of the caldera and produced a total of 3 cm of inflation (Figure 6c). Given the long time span of periods 2 and 3, 672 and 168 days, respectively, the subsidence within the rift zones observed during period 1 is still present (Figures 6b and 6c). During period 4, the center of inflation shifted back to the inner caldera source and inflated a total of 4 cm in 24 days (Figure 6d). For all three periods, the horizontal GPS displacements around the summit (stations UWEV and AHUP) were radially outward, while stations on the flank and rift zones (stations KOSM and MANE) continued to exhibit the same seaward motion seen during period 1.

[15] Period 5 (Figure 6e) marks a shift in the center of inflation from the inner caldera to an area outside and to the south-southeast of the caldera. Coincident with a seismic swarm in the upper east rift zone, a maximum displacement of 11 cm occurred in an area centered between the upper portions of the east and southwest rift zones during this 48 day period. The high rate of inflation was sustained until 28 March 2006, at which point the inflation shifted to an area outside and to the south-southwest of the caldera, marking the beginning of period 6 (Figure 6f). Inflation during period 6 lasted for approximately 6 months with a maximum of 14 cm, and occurred as a broad area with an elongated pattern extending toward the southwest rift zone. During periods 5 and 6, station KOSM switched from southeast to southwest motion, and station UWEV shifted more to the north for period 5 and returned to northwest motion during period 6. Following period 6, there is no clear evidence of inflation around the summit for the latter part of 2006 and into the beginning of 2007, and seismic activity returned to normal background levels.

[16] Another shift in the center of inflation occurs during period 7 (Figure 6g) as inflation returned to the area previously seen during period 5, accompanied by an increase in seismic activity in the upper east rift zone. On 24 May 2007, an M 4.7 earthquake occurred in the upper east rift zone near Puhimau Crater at 2 km depth followed by M 4.1 and M 3.9 aftershocks further down–rift at 3.3 km and 1.0 km depth, respectively (white stars, Figure 6g). The maximum amount of uplift during period 7 was 5 cm (Figure 6g), less than half the amount during period 5. The GPS stations around the summit show a radially outward pattern and the stations on the south flank continue to show southeast motion (Figure 6g).

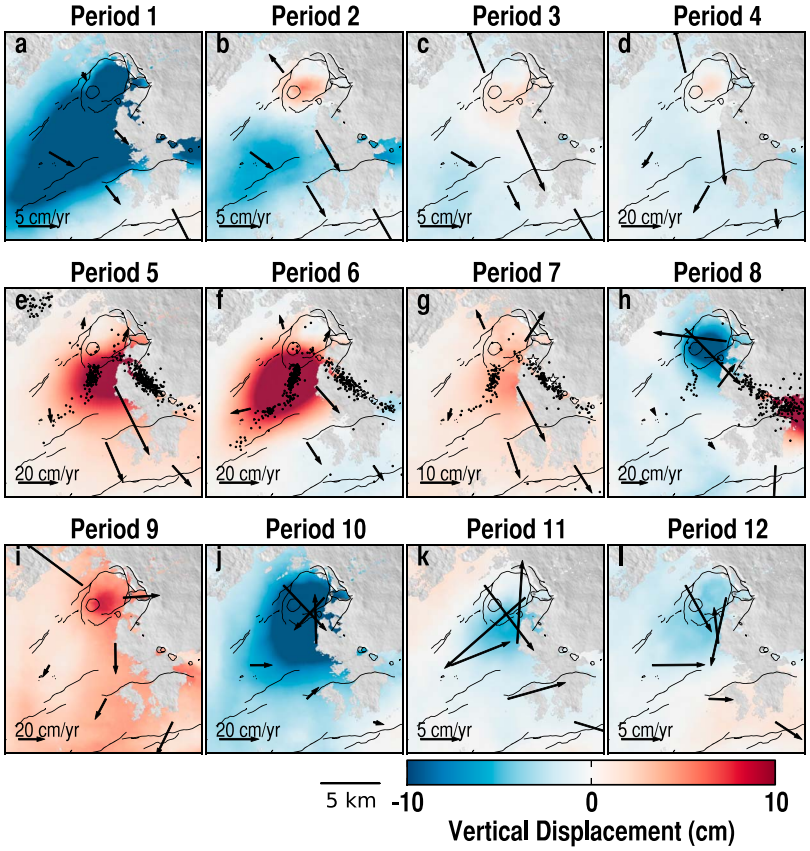

Figure 6. (a–l) Vertical displacement maps for the 12 defined time periods between January 2000 and March 2008 (Table 1) showing the shifts in the center of deformation during this time. Arrows represent the horizontal GPS velocity vectors for the stations labeled in Figure 1. The black dots shown in Figures 6e–6h are the earthquake locations during swarm activity described in the text. The color scale for all periods is plotted with the same range (−10 to +10 cm). The scale for the arrows showing horizontal GPS velocities varies (between 5 cm/yr and 20 cm/yr).

3.3. East Rift Zone Intrusion and Eruption: Periods 8 and 9

[17] The 17 June 2007 intrusion and eruption in the upper east rift zone created large amounts of ground displacement between the summit and Pu‘u ‘Ō‘o (Figure 5i) [*Sandwell et al.*, 2008; *Montgomery-Brown et al.*, 2010]. Period 8 is characterized by 16 cm of subsidence concentrated inside the summit caldera to the northeast of Halemaumau (Figure 6h). The intrusion produced over 30 cm of uplift in the vicinity of the intrusion and eruption (see Figure 5i) accompanied by swarms of earthquakes over the first several days of the event. The GPS stations around the summit show radially inward motion in response to the rapid subsidence at the summit (Figure 6h). Period 9 is characterized by an inflation of 6 cm in a small concentrated area to the northeast of Halemaumau, and the GPS stations around the summit show a radially outward pattern (Figure 6i). The entire area surrounding the summit appears red, and is most likely related to the atmospheric noise discussed above.

3.4. Summit Deflation: Periods 10 Through 12

[18] Following the intrusion and eruption in the east rift zone, the summit area entered an episode of net subsidence comprising three time periods (Figures 6i–6l) and seismic activity returned to background levels. The location of displacement shifted position during this time from the inner caldera to the southeastern edge of the caldera. Period 10 is characterized by a broad area of subsidence spanning the inner caldera and southeastern portion of the summit with a maximum of 15 cm centered on the southeastern edge of the caldera (Figure 6j). A change in the rate of subsidence occurred during Period 11 evident from the change in slope in the GPS and InSAR time series (see Figure 4, note stations AHUP and UWEV). The period is characterized by a subsidence of 6 cm located just outside the southeastern edge of the caldera. Unlike periods 10 and 11, period 12 (Figure 6l) lacks a well-defined location of maximum displacement and is characterized by a broad area of subsidence both inside and outside the caldera with a maximum displacement of 4 cm.

3.5. Sources of Deformation

[19] We infer the areas of displacement active during periods 2 through 11 to be associated with four distinct sources. The time variation of the surface displacement patterns and the locations of these different sources are best visualized with maps showing the contoured vertical displacements (Figure 7). Source 1 is located in the inner

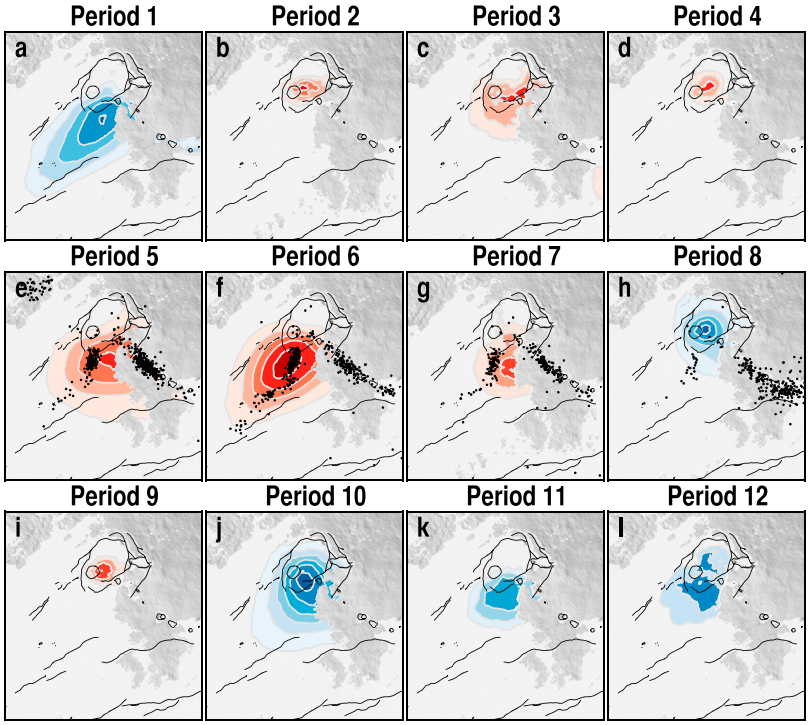

Figure 7. (a–l) Contours of the vertical displacement for the 12 defined time periods (same as in Figure 6). The contour interval varies in order to emphasize the location of maximum displacement and the active magma source. The four areas of deformation corresponding to magma bodies include an inner caldera source (source 1, periods 2, 4, 8, and 9), a source on the southern edge of the caldera (source 2, periods 3 and 10), a source to the south-southeast of the caldera (source 3, periods 5, 7, and 11), and a source to the south-southwest of the caldera (source 4, period 6). The black dots shown in Figures 7e–7h are the earthquake locations during swarm activity described in the text.

caldera to the northeast of Halemaumau Crater and is active during periods 2, 3, 8, and 9 (Figures 7b, 7d, 7h, and 7i). This source is best described as a concentrated area of displacement confined to the inner caldera with periods of both uplift and subsidence. Source 2 is active during periods 4 and 10 (Figures 8c and 7j), and is located on the southern edge of the caldera. The area of displacement for this source is not as concentrated as source 1, and the displacement occurs over an area that spans both inside and outside the summit caldera. Source 2 shows uplift during period 4 and subsidence during period 10. Source 3 is located to the south-southeast of the summit caldera and was active during periods 5, 7, and 11 (Figures 7e, 7g, and 7k, respectively) and shows both uplift and subsidence during these periods. This source is characterized by a broad area of displacement located completely outside the summit caldera and contained within an area between the upper rift zones and to the northeast of the Koae fault system. Source 4 is located to the south-southwest of the summit caldera and is only active during period 6 (Figure 7f). The source shows a broad area of uplift outside the summit caldera that was elongated down the southwest rift zone.

4. Source Modeling

4.1. Methods

[20] The surface displacement field shows short wavelengths and localized patterns of displacement, consistent with shallow, magmatically induced deformation. To determine the sources of the observed displacements, we employed the following modeling strategy. We select, for each source, the period with the highest signal-to-noise ratio of the data. We acknowledge that modeling of only one time rather than modeling all time periods may be selective, but this provides a first-order approach to reducing errors in the modeling by only using the best data available for each source. We test models with increasing complexity and use geophysical inversion methods to select the model parameters that best fit the observations. We start with a Mogi point source [*Mogi*, 1958] to simulate a spherical magma chamber. For sources that do not provide a good fit with the Mogi model, we use penny-shaped crack [*Fialko et al.*, 2001] or horizontal uniform rectangular dislocation [*Okada*, 1985]. These sources simulate horizontal, radially symmetric and elliptical sills, respectively. In all models, we assumed homogeneous, elastic half-space with a Poisson's ratio of 0.25 and shear modulus of 3×10^{10} Pa.

[21] We run a Mogi point source model for each time period to find approximate horizontal locations, and the results show good agreement for four distinct sources. The individual time periods we use for more robust modeling of the four sources in more detail are selected to minimize adverse effects of noisy data and possible contributions from secular deformation. This requires the periods to have short time spans and clear deformation from only one source. Out of the four possible periods for source 1 (periods 2,4,8,9),

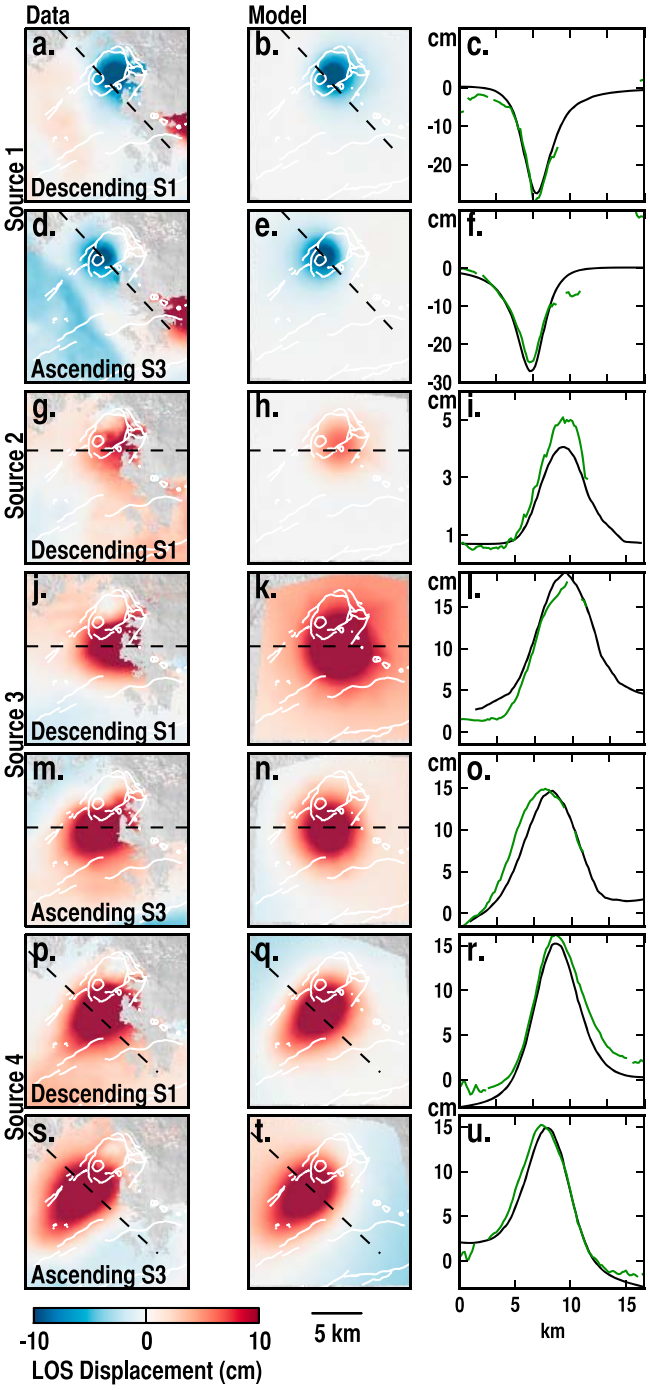

Figure 8. (a–u) Best fitting model results for the four identified magma bodies beneath Kīlauea. The four time periods used for modeling were selected to minimize time span and signal to noise levels. Profiles show the fit of the model (black line) to the data (green line). Profile locations are marked by dashed lines.

period 8 is selected because it had a 24 day time span and large displacement signal with over 15 cm of subsidence. Out of the two possible periods for source 2 (periods 3 and 10; before and after the east rift zone intrusion and eruption), period 3 is selected because period 10 likely contains contributions from other sources. Out of the three possible periods for source 3 (periods 5, 7, 11), period 5 is selected for modeling because it provides the largest signal with the shortest time span. Source 4 is only active during period 6.

[22] The modeling is done using the ascending and descending SBAS displacements for each period. We use quadtree decomposition sampling of the data as modeling input to reduce redundant data [*Jonsson et al.*, 2002]. Using quadtree partitioning, we allow a minimum of two and a maximum of seven partitioned levels and variance thresholds between 5 and 10 mm between data points that results in a minimum of 16 data points and a maximum of 16,384. The quadtree sampling results in 86 and 62 data points for the ascending and descending displacements for modeling source 1, 177 data points for the descending displacement for source 2, 82 and 69 points for the ascending and descending displacements for source 3, and 108 and 83 points for the ascending and descending displacements for source 4. The GPS data are excluded from modeling due to sparse station spacing during this time period, which results in poor coverage of the deformation sources (Figure 6). Most areas containing the highest amounts of displacement are not well covered by any of the GPS stations with the exception of source 3 (station AHUP, Figure 6). Since 2008, new stations have been installed in and around the summit caldera that improves the coverage provided by continuous GPS.

[23] To determine the best fitting model, we assume unit variance for all data points and use the normalized root-mean-square (RMS) between the data and the model defined as sqrt((d-m)2/N) where d is the data, m is the model, and N is the number of data points. We solve this nonlinear inversion problem using a Gibbs sampling algorithm. The Gibbs sampling uses a similar algorithm as for simulated annealing [*Cervelli et al.*, 2001], except we invert for a large number of models. Gibbs sampling generates a distribution for each parameter and provides the joint distribution. We obtain posterior probability density distributions of the parameters for the preferred model from the sampling. This set of models is a proxy for the posterior probability density that allows us to evaluate the desired quantities such as mean and confidence intervals.

4.2. Results

[24] Table 2 contains the modeled parameters for each of the sources, and shows the preferred depths and 95% confidence interval obtained from the Gibbs sampling. The depths for each of the sources refer to the distance below the surface.

[25] The best fitting model for source 1 is a point source (Figures 8b and 8e), rather than a sill geometry, and is located to the northeast of Halemaumau Crater inside the summit caldera at a depth of 1.9 $\pm$ 0.1 km. The estimated volume loss for this period is 9.1 $\times$ 10^6 m^3. The best fitting model for source 2 (Figure 8h) is penny-shaped crack located close to the southeast edge of the caldera at a depth of 2.9 $\pm$ 0.2 km with a radius of 2.3 $\pm$ 0.2 km and a volume increase of 8.9$\times$$10^6$ m^3. The best fitting model for source 3 (Figures 8k and 8n) is a penny-shaped crack located to the south-southeast of the caldera between the east and southwest rift zones at a depth of 3.4 $\pm$ 0.5 km with a radius of 3.4 $\pm$ 0.6 km and a volume increase of 11.8 $\times$ 10^6 m^3. The location and size of the source places the outer edges of the sill adjacent to the seismicity within the rift zones with

Table 2. Model Parameters for the Four Sources at the Summit of Kīlauea

Source	Modeled Period	Model Type	Depth/95% CI (km)	Radius/95% CI (km)	Area (km^2)	Latitude, Longitude	ΔV^a (10^6 m^3)
1	8	Mogi	1.9/1.87–2.07			19.4069, −155.2752	−9.1
2	3	Penny	2.9/2.5–3.3	2.3/2.0–2.7		19.3961, −155.2700	8.9
3	5	Penny	3.6/2.7–4.7	3.0/1.3–4.0		19.3838, −155.2710	11.8
4	6	Okada	3.6/2.9–4.2		14.8	19.3819, −155.2891	10.9

[a]Change in source volume, increase is positive.

little to no overlap between the two. The best fitting model for source 4 (Figures 8q and 8t) is a uniform dislocation with an overall area of 14.8 km^2 at a depth of 3.6 ± 0.4 km and an estimated volume increase of 10.9×10^6 m^3. The depth is in the same range as source 3, but the location is further to the west and the pattern of displacement is different as well, exhibiting an elongated shape extending toward the southwest rift zone. Profiles comparing the modeled source with the data show good agreement (Figure 8, right column).

[26] Probability density distributions of latitude and longitude (point clouds, Figure 9a) and depth (histograms, Figure 9b) from the modeling clearly show four distinct source locations. From source 1 to source 4, the source location generally progresses from north to south and from shallow to deep. The centers of sources 1, 2, and 3 overlap, or align, in east-west extent while source 4 is farther to the west. Sources 1 and 3 have very localized point clouds showing well-constrained horizontal locations. Source 2 has a broad range of depths and a larger spread in locations, which is reasonable given the lower signal-to-noise ratio of the data. Source 4 also has a larger spread in locations, but the depth is well constrained.

[27] Figure 10 shows the correlation between the estimated source size and depth (Figure 10a) and the differences in horizontal overlap progressing from the lower 95% confidence bound (L95) to the upper bound (U95) for sources 2, 3, and 4 (Figure 10b). Source 1 has the least variation in depth. The size of source 1 is not inferred from the data or modeling, so for Figure 10b, we assume a constant radius of 500 m for source 1. In general, the relation between depth and source size shows that sources are either deep and small or large and shallow. This correlation is strongest for source 3 (Figure 10a, middle), with no obvious trend for sources 2 and 4. The mean of the posterior density distribution (for both depth and radius) is the preferred model and is shown as stars in Figure 10a.

[28] The source depth as a function of time is shown in Figure 11. From 2004 leading up to the 2007 intrusion and eruption (Figure 11, vertical red line), the summit area inflated and showed a general progression from shallow to deeper sources through time (periods 2–7). Concurrent with the intrusion and eruption, the shallow summit source deflated (period 8) followed by a short period of inflation (period 9) and then continued deflation (periods 10–12), again showing a progression from shallow to deeper sources through time. This sequence represents a top-down inflation and deflation of the shallow summit reservoirs.

5. Discussion

[29] The deformation at the summit of Kīlauea Volcano shows a time variable pattern of displacement between 2000 and 2008. The locations and timing of displacements provide details about the characteristics of the shallow magmatic system beneath the summit.

5.1. Model for the Shallow Magmatic System

[30] We suggest that the shallow magmatic system at the summit of Kīlauea is best described as a series of interconnected reservoirs that are active at different points in time. We find four distinct deformation sources active between October 2003 and March 2008, with varying locations and times of activity (Table 1). Figure 12 depicts a schematic cross section across the summit and upper east rift zone of Kīlauea. The schematic is not to scale and is intended to show the relative locations of the modeled sources beneath the summit. Although the elastic half-space models fit the data, questions still remain about whether sills of this size are geologically feasible at Kīlauea. The sources get progressively deeper from north to south. Sources 2, 3, and 4 are best fit with sill-type models, whereas source 1 is best fit with a spherical model (Mogi). The inferred sources are consistent with other studies of the same period. *Poland et al.* [2009] and *Montgomery-Brown et al.* [2010] both found a point source at 1.5 km depth to the northeast of Halemaumau, which matches well with our source 1. *Myer et al.* [2008] modeled the same time period we have for sources 3 and 4 (periods 5 and 6) as a single source and found a similar oblong-shaped source. Their source location matches well with our source 4, except they found a shallower depth. We interpret the observed deformation to be related to magmatic processes and not hydrothermal activity due to our source depths being much deeper than the known hydrothermal system, which is thought to be shallower than 1 km [*Almendros et al.*, 2001; *Hurwitz and Johnston*, 2003], and also the fact that the deformation correlates with ongoing magmatic and volcanic activity at Kīlauea.

[31] The shallow magmatic system consists of a shallow reservoir (1.9 ± 0.1 km depth) to the northeast of Halemaumau (source 1) and a series of vertically stacked sills at greater depths (2.5–4 km) (source 2, 3, and 4). The level of neutral buoyancy (LNB) at Kīlauea occupies a zone from 2 to 4 km [*Ryan*, 1987], and this corresponds well with the depths we find for our four sources. Mantle-derived magma enters the system from below and rises up to shallow depths. As the supply of magma continues and reaches the LNB, magma begins to migrate laterally, creating individual sills in this depth range. These reservoirs appear to be well connected at times, yet show individual periods of activity. This suggests the connections or pathways between the magma bodies are either small and rapid changes in pressure only affect one reservoir at a time, or the connections are not continuously open and changes in pressure and stress of the system effectively open and close the pathways. The ongoing eruptive activity at Pu‘u ‘Ō‘o provides evidence that magma continuously migrated away from the summit during this time.

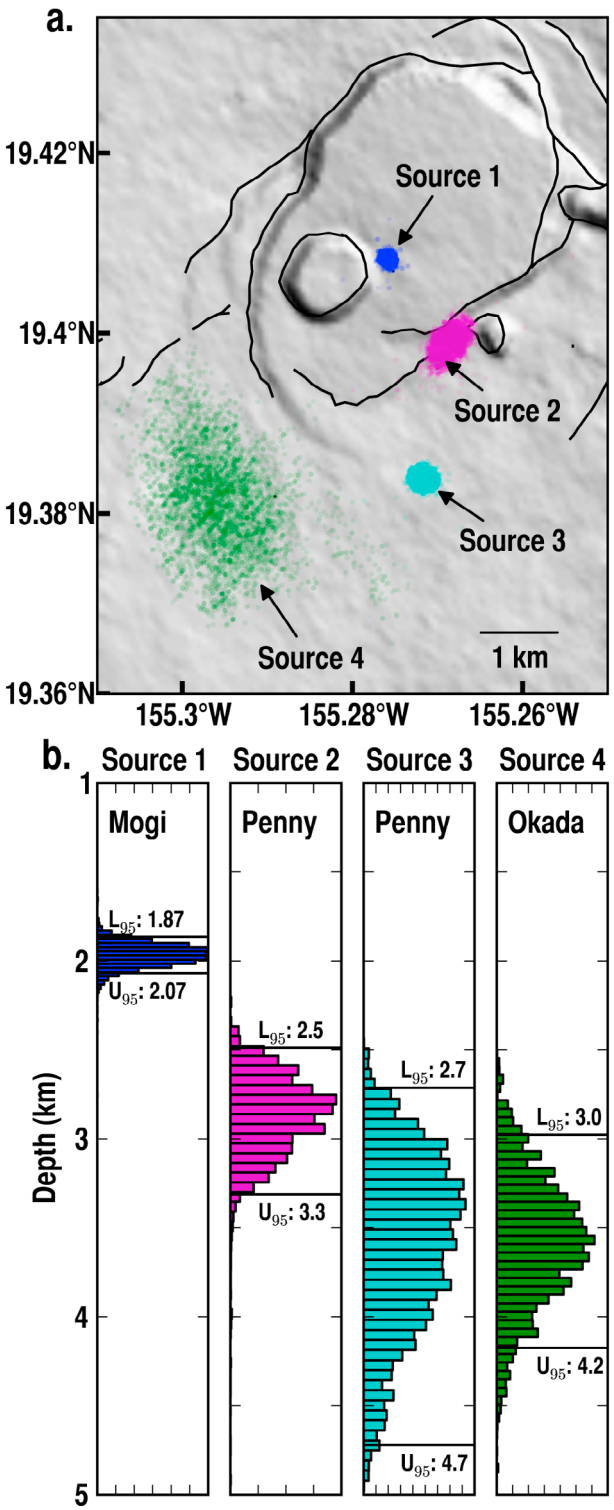

Figure 9. Map of the modeled sources around the summit caldera. (a) Two-dimensional scatterplot of the latitude and longitude positions for the four sources showing the locations in and around the summit caldera. (b) Normalized marginal probability density distributions of depths from the Gibbs sampling. The black lines indicate the lower (L95) and upper (U95) bounds of the 95% confidence interval.

5.2. Top-Down Inflation and Deflation

[32] The time dependence of magma storage is apparent when looking at the sequence of source initiation (Figure 13; see also Figure 11). After sources 1 and 2 inflated (Figure 13a, periods 2 to 4), the 2006 upper east rift seismic swarms (periods 5) mark when magma began accumulating at the summit in the deeper sill bodies (Figure 13b, sources 3 and 4). These magma bodies continued to inflate into the beginning of 2007 (period 6), when inflation around the summit ceased. Summit activity resumes with the inflation of source 3 (period 7), coincident with an increase of the seismicity in the upper east rift zone. The associated seismicity at ~3 km depth below the surface suggests that the conduit into the upper east rift zone originates at the depth of or slightly below source 2. The 2007 dike is fed by magma from source 1, as evidenced by rapid deflation of this source (Figure 13c). After a brief pulse of inflation of source 1, which may represent a rebound effect following the rapid pressure changes, source 2 deflates followed by the deflation of source 3 (Figure 13d).

[33] The summit sources clearly show a sequence of filling and emptying from the top down (shallow to deep) as

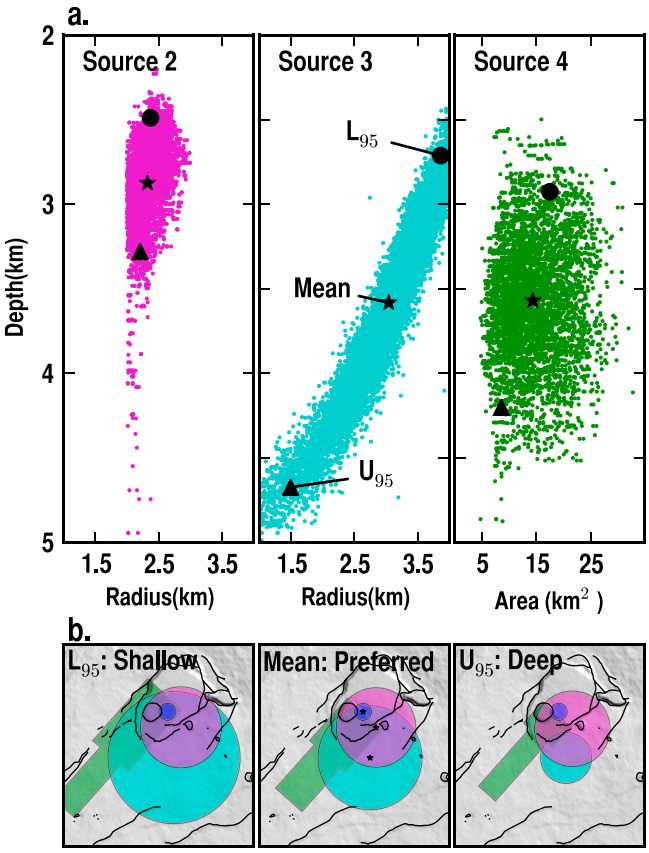

Figure 10. (a) Two-dimensional scatterplot from the Gibbs sampling representing the posterior probability distribution as a function of source depth and size (radius for sources 2 and 3, area for source 4). Circles, stars, and triangles represent the lower confidence bound (L95), mean of the Gibbs sampling, and upper confidence bound (U95), respectively. (b) Spatial distribution of sources for the points in Figure 10a. Source 1 (blue circle) is plotted with a constant radius of 500 m, and the colors and sources are the same as in Figure 9.

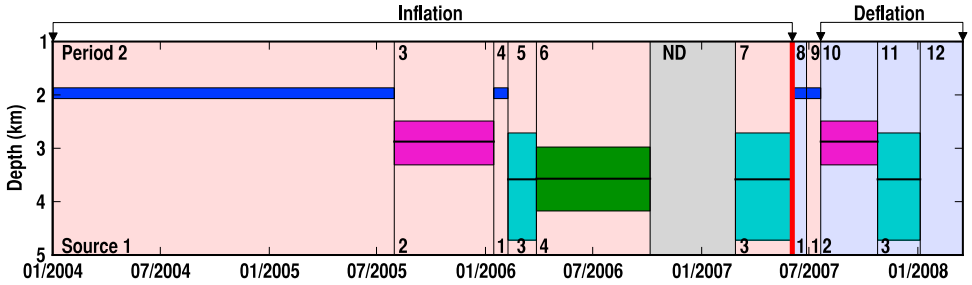

Figure 11. Source depth versus time for the four sources (red background indicates inflating sources, blue is deflating). Vertical lines separate the time periods listed in Table 1. Vertical red line marks the beginning of the period for the June 2007 intrusion and eruption. ND is a time with no deformation as seen in the InSAR-GPS time series (Figure 4, between periods 6 and 7). Black horizontal lines in the middle of each source mark the mean depth and the widths are the 95% confidence interval.

magma enters and leaves the system, respectively. The shallow sources are the first to inflate beginning in late 2003, and are the first to deflate following the 2007 intrusion and eruption. In a hydraulically connected system at neutral buoyancy we would expect simultaneous pressurization and depressurization of all sources with the volume change depending on the source compressibility [*Rivalta and Segall*, 2008]. This is in contrast to our observations, which suggests that the system is not fully hydraulically connected. The deeper sources may inflate only if the excess pressure exceeds a given threshold to open the conduit to these sources. In the same way, these sources deflate only once the excess pressure in the main plumbing system has dropped below a given threshold. This limited hydraulic connectivity could also be an expression of the conduit size. The conduits from the deeper sources to the east rift zone could be much smaller than those from the shallower sources, impeding the rapid equilibration of pressure changes for the deeper sources. The importance of conduit size for Kīlauea's intrusions was first noted by *Segall et al.* [2001].

[34] Previous periods of activity at Kīlauea are consistent with the top-down inflation that we observed in this study. *Fiske and Kinoshita* [1969] found the shallow source next to Halemaumau was the first to inflate prior to the 1967–1968 eruption, followed by deeper sources to the south of the caldera. This same sequence of inflating sources occurred from 2003 to 2007 leading up to the 2007 east rift zone intrusion and eruption. Periods of inflation at Kīlauea show a general trend of source migration from northeast of Halemaumau toward the south [*Tilling and Dvorak*, 1993]. The sources inside the caldera are shallower than those to the south, so we infer that top-down inflation is a general pattern for Kīlauea given that the inner caldera sources inflate first, followed by the south caldera sources.

5.3. Secular Deformation

[35] The summit and upper rift zones subsided at a constant rate during period 1, with the maximum rate of 4–5 cm/yr just south of the summit caldera (period 1, Figure 5a, 5b, and 5c). It is evident that subsidence continued within the upper rift zones following this period as seen in the GPS (station KOSM, Figure 4), but subsidence close to the summit is overprinted by the inflation of the shallow magmatic system (periods 2 through 7). At the location of the

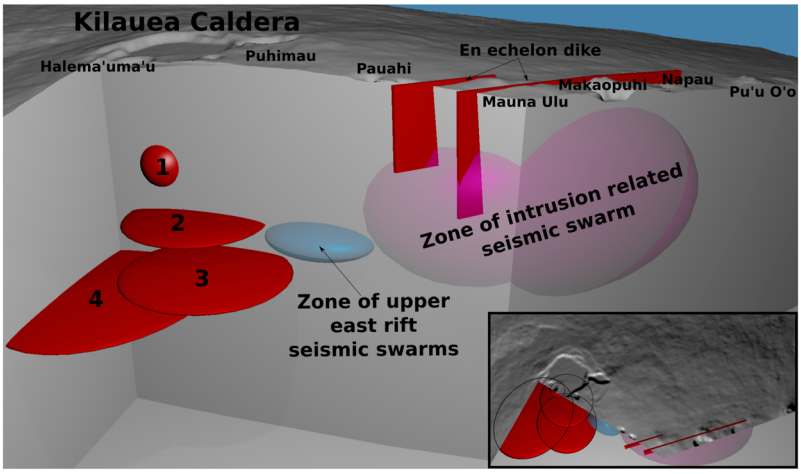

Figure 12. Schematic cross section (not to scale) across the summit and east rift zone of Kīlauea showing details of the shallow magmatic system. The modeled sources (Table 2) are shown as red bodies beneath the summit caldera. The en echelon dike depicts the 2007 intrusion and eruption detailed by *Montgomery-Brown et al.* [2010].

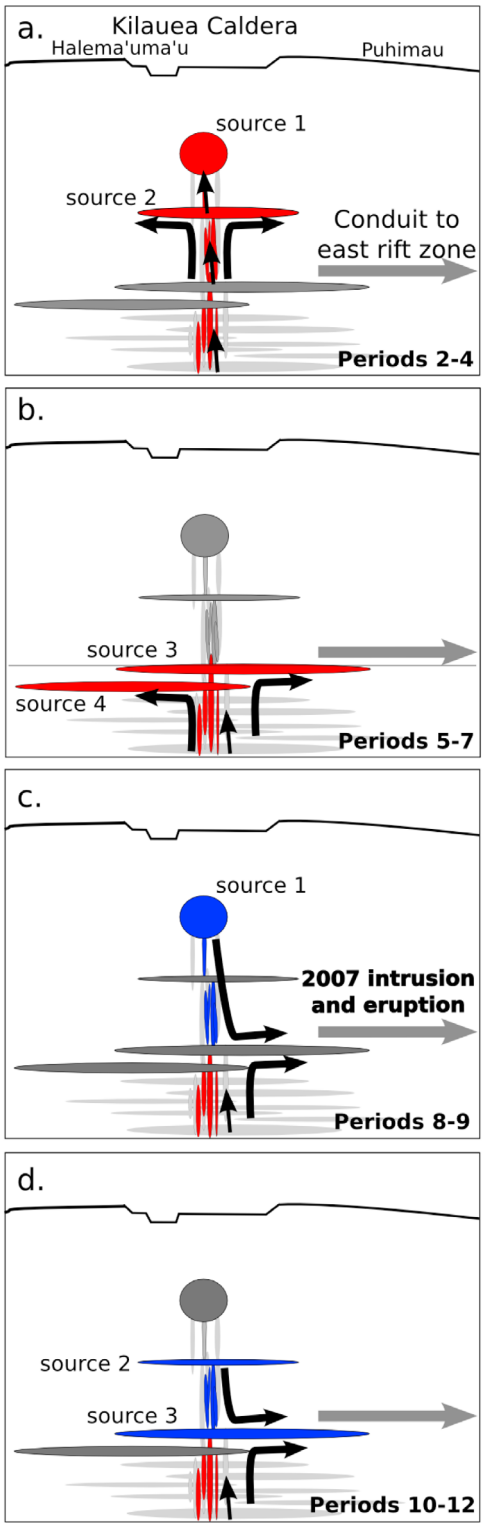

Figure 13. (a–d) Schematic sequence of the top-down inflation-deflation beneath the summit of Kīlauea (not to scale). Arrows represent the magma migration paths. Red sources indicate inflation and blue sources indicate deflation. Tables 1 and 2 list details about the time periods and source locations, respectively.

2007 east rift zone dike, subsidence related to the secular deformation is observed before and after the intrusion (Figures 5f and 5l). *Delaney et al.* [1998] found similar patterns of subsidence from 1976 to 1996 using repeated leveling surveys. We suggest that the secular deformation is predominately the result of tectonic processes with a lesser contribution from magmatic processes, consistent with the changes of gravity in that area [*Johnson et al.*, 2010]. During period 1, the GPS stations on Kīlauea's flank show a steady seaward movement [*Miklius et al.*, 2005], providing further evidence of tectonic processes resulting in rifting and secular deformation.

5.4. Comparison With Previous Studies of Summit Magma Bodies

[36] Previous geodetic studies of the shallow magmatic system at Kīlauea using leveling, tilt, trilateration, and GPS for earlier periods of activity also detected multiple reservoirs between 1 and 4 km depths (Table 3). *Fiske and Kinoshita* [1969] found multiple centers of inflation in and around the summit caldera from 1966 to 1967. They concluded that a complex reservoir system existed beneath Kīlauea's summit consisting of sources located to the northeast of Halemaumau and along the southern edge of the caldera between 2 and 3 km depth. *Dvorak et al.* [1983] located 25 centers of activity at the summit from 1966 to 1970. Their models placed sources inside the caldera to the northeast of Halemaumau at 2.2 and 2.6 km depth and just to the south of the caldera at 2.4 and 3.4 km depth. *Yang et al.* [1992] reexamined data from 1975 to 1985 and found 10 centers of deflation located under the southern caldera rim in the same area as our sources 2 and 3. They identified inflation centers located in the same areas as our sources 1, 2, and 3, but modeled these as a single inflation source and incorporated dikes into their models as well. They note that neglecting to account for dike dislocations could affect the estimated centers of inflation. From 1981 to 1985, *Johnson* [1992] inferred deflation sources at 2.5 km depth to the northeast of Halemaumau and deeper deflation sources at 3.5 and 4 km depth further to the south, closer to the southwest rift zone. He placed the deflation source associated with the 1983 east rift intrusion, which marked the beginning of the eruptive activity that continues today, just north of the southern caldera rim. *Wallace and Delaney* [1995] place a deflation source associated with the same intrusion just south of the caldera rim (near our source 2) at a depth of 3.8 $\pm$ 1 km. *Owen et al.* [2000] used GPS displacements to model the deflation of a shallow caldera source at a depth of 1.87 km coincident with the 1997 Napau Crater dike intrusion and eruption. In 2000–2002, *Cervelli and Miklius* [2003] used electronic borehole tiltmeter data of four $\sim$2 day interval tilt events to infer a source near Halemaumau (same horizontal position as our source 1) at a depth of 500–700 m below the surface. Using leveling and GPS data from 1996 to 2002, they also inferred a long-term deflation source at 3.5 km depth.

[37] Although many of these studies were limited in spatial and temporal coverage, collectively they support the idea that the magmatic sources, which we observed from late 2003–2008, are persistent features with different instances of activity (Table 3). Source 1 agrees well with the caldera source observed by *Fiske and Kinoshita* [1969]. This source

Table 3. Summit Sources From Previous Studies and Relationship to This Study

Activity	Time Period (month/year)	Source Location	Depth (km)	Reference Study	Inferred Source[a]
Summit inflation, rapid extension, and swarms	12/1973–4/1974; 1/1966–1/1967; 1/1967–10/1967; 1/1967–2/1967	Halemaumau[b]; Halemaumau[b]; South caldera[b]; South caldera[b]	2.15; 2; 3; 2.59	*Dvorak et al.* [1983]; *Fiske and Kinoshita* [1969]; *Fiske and Kinoshita* [1969]; *Dvorak et al.* [1983]	1; 1; 2, 3, and 4; 2 and 3
Summit inflation and deflation	1970–1985	South caldera[c]	2.6	*Yang et al.* [1992]	2
Southwest rift zone swarm	2/1982	South caldera[d]	7.2 ± 4.4	*Wallace and Delaney* [1995]	2
East rift zone intrusion	1/1983	South caldera[d]; South caldera[d]	3.5; 3.8 ± 1.0	*Johnson* [1992]; *Wallace and Delaney* [1995]	2; 2
Pu‘u ‘Ō‘o Eruptions	4/1985–12/1985	Halemaumau[d]	2.5	*Johnson* [1992]	1
East rift zone intrusion	1/1997	Halemaumau[d]	1.87	*Owen et al.* [2000]	1
Summit tilt events	1/2000–1/2002	Halemaumau[b]	0.5–0.7	*Cervelli and Miklius* [2003]	1
Long-term subsidence	1/996–1/2002	South caldera[d]	3.5	*Cervelli and Miklius* [2003]	4
Summit inflation	2/2006–10/2006	South caldera[b]	2	*Myer et al.* [2008]	4
2007 intrusion and eruption	6/2007	Halemaumau[d]	1.5; 1.5	*Poland et al.* [2009]; *Montgomery-Brown et al.* [2010]	1

[a]This study.
[b]Inflating source.
[c]Inflating and deflating source.
[d]Deflating source.

was active throughout the 1960s and 1970s, and before and after the 1983 east rift intrusion [*Dvorak et al.*, 1983; *Johnson*, 1992]. It was also active during the 1997 intrusion [*Owen et al.*, 2000]. Source 2 was likely active during the pre-1983 period and was the main deflation source associated with the 1983 intrusion [*Johnson*, 1992; *Wallace and Delaney*, 1995]. Sources 3 and 4 have less frequent periods of activity and were observed during 1967–1983 [*Fiske and Kinoshita*, 1969; *Dvorak et al.*, 1983]. The locations of sources 3 and 4 are similar to that of the long-term source of *Cervelli and Miklius* [2003]. Their 1996–2002 leveling-measured subsidence pattern (Figure 5 in *Cervelli and Miklius* [2003]) is nearly identical to our 2000–2004 InSAR-observed secular deformation pattern (Figure 8a). We interpret that the source of subsidence is primarily related to the tectonic processes discussed above with a lesser component related to the shallow magmatic sources.

6. Conclusions

[38] This study provides details of the activity at the summit of Kīlauea Volcano, Hawai‘i, as follows:

[39] 1. We use InSAR time series analysis of Radarsat-1 data from 2000 to 2008 to describe the activity related to the migration of magma beneath the summit of Kīlauea. The shallow magmatic system consists of an interconnected system of four magma bodies progressing in depth from north to south. It includes a spherical reservoir to the northeast of Halemaumau at 1.9 ± 0.1 km depth and a series of vertically stacked sills to the south of the caldera at greater depths (2.9 ± 0.2 to 3.6 ± 0.4 km). The sills overlap laterally but have distinct periods of activity, leading to the conclusion that these are independent magma bodies with varying times of activity.

[40] 2. Deformation just south of the summit caldera (area of sources 2, 3, and 4) and the seismicity in the upper rift zones provide key insights into the migration of magma at the summit. The location of earthquake swarms outlines conduits or pathways for magma migration away from the summit.

[41] 3. The timing of source activity reveals a top-down (shallow to deep) inflation before and top-down deflation following the 2007 east rift zone intrusion and eruption. This general pattern of top-down inflation has been seen previously, and the same sequence for deflation is clearly seen in the InSAR time series analysis as well.

[42] **Acknowledgments.** NSF provided funding for tasking and purchasing the Radarsat-1 data and graduate assistantship for Baker. The authors would also like to thank Tim Dixon and Shimon Wdowinski for thoughtful discussions about technical and scientific details and proofreading drafts of the manuscript. We would also like to acknowledge Mike Poland for his detailed review and comments that helped to improve the manuscript.

References

Almendros, J., B. Chouet, and P. Dawson (2001), Spatial extent of a hydrothermal system at Kilauea Volcano, Hawaii, determined from array analyses of shallow long-period seismicity 2. Results, *J. Geophys. Res.*, *106*(B7), 13,581–13,597, doi:10.1029/2001JB000309.

Amelung, F., S. Jónsson, H. Zebker, and P. Segall (2000), Widespread uplift and “trapdoor” faulting on Galápagos volcanoes observed with radar interferometry, *Nature*, *407*, 993–996, doi:10.1038/35039604.

Amelung, F., S. Yun, T. R. Walter, P. Segall, and S. Kim (2007), Stress control of deep rift intrusion at Mauna Loa volcano, Hawaii, *Science*, *316*, 1026–1030, doi:10.1126/science.1140035.

Berardino, P., G. Fornaro, R. Lanari, and E. Sansosti (2002), A new algorithm for surface deformation monitoring based on small baseline differential SAR interferograms, *IEEE Trans. Geosci. Remote Sens.*, *40*, 2375–2383, doi:10.1109/TGRS.2002.803792.

Cervelli, P., and A. Miklius (2003), The shallow magmatic system of Kilauea Volcano, in the Pu‘u ‘Ō‘o-Kūpaianaha eruption of Kīlauea Volcano, Hawai‘i: The first 20 years, *U.S. Geol. Surv. Prof. Pap.*, *1676*, 149–163.

Cervelli, P., M. Murray, P. Segall, Y. Aoki, and T. Kato (2001), Estimating source parameters from deformation data, with an application to the March 1997 earthquake swarm off the Izu Peninsula, Japan, *J. Geophys. Res.*, *106*(B6), 11,217–11,238, doi:10.1029/2000JB900399.

Chadwick, W. W., D. Geist, S. Jonsson, M. Poland, D. Johnson, and C. Meertens (2006), Volcano bursting at the seams: Inflation, faulting, and eruption at Sierra Negra volcano, Galapagos, *Geology*, *34*, 1025–1028, doi:10.1130/G22826A.1.

Dawson, P., D. Whilldin, and B. Chouet (2004), Application of near real-time radial semblance to locate the shallow magmatic conduit at Kilauea Volcano, Hawaii, *Geophys. Res. Lett.*, *31*, L21606, doi:10.1029/2004GL021163.

Delaney, P. T., R. P. Denlinger, M. Lisowski, A. Miklius, P. G. Okubo, A. T. Okamura, and M. K. Sako (1998), Volcanic spreading at Kilauea, 1976–1996, *J. Geophys. Res.*, *103*(B8), 18,003–18,023, doi:10.1029/98JB01665.

DeMets, C., R. G. Gordon, D. F. Argus, and S. Stein (1994), Effect of recent revisions to the geomagnetic reversal time scale on estimates of current plate motions, *Geophys. Res. Lett.*, *21*, 2191–2194, doi:10.1029/94GL02118.

Dvorak, J., A. Okamura, and J. H. Dieterich (1983), Analysis of surface deformation data, Kilauea Volcano, Hawaii October 1966 to September

1970, *J. Geophys. Res.*, *88*(B11), 9295–9304, doi:10.1029/JB088iB11p09295.

Fialko, Y., Y. Khazan, and M. Simons (2001), Deformation due to a pressurized horizontal crack in an elastic half-space, with applications to volcano geodesy, *Geophys. J. Int.*, *146*, 181–190, doi:10.1046/j.1365-246X.2001.00452.x.

Fiske, R. S., and W. T. Kinoshita (1969), Inflation of Kilauea Volcano prior to its 1967–1968 eruption, *Science*, *165*, 341–349, doi:10.1126/science.165.3891.341.

Gourmelen, N., F. Amelung, and R. Lanari (2010), Interferometric synthetic aperture radar-GPS integration: Interseismic strain accumulation across the Hunter Mountain fault in the eastern California shear zone, *J. Geophys. Res.*, *115*, B09408, doi:10.1029/2009JB007064.

Heliker, C., D. A. Swanson, and T. J. Takahashi (2003), The Pu'u 'Ō'o-Kūpaianaha eruption of Kilauea Volcano, Hawaii: The first 20 years, *U.S. Geol. Surv. Prof. Pap.*, *1676*.

Hurwitz, S. and M. J. S. Johnston (2003), Groundwater level changes in a deep well in response to a magma intrusion event on Kilauea Volcano, Hawai'i, *Geophys. Res. Lett.*, *30*(22), 2173, doi:10.1029/2003GL018676.

Johnson, D. (1992), Dynamics of magma storage in the summit reservoir of Kilauea Volcano, Hawaii, *J. Geophys. Res.*, *97*(B2), 1807–1820, doi:10.1029/91JB02839.

Johnson, D. J., A. A. Eggers, M. Bagnardi, M. Battaglia, M. P. Poland, and A. Miklius (2010), Shallow magma accumulation at Kilauea Volcano, Hawai'i, revealed by microgravity surveys, *Geology*, *38*, 1139–1142, doi:10.1130/G31323.1.

Jonsson, S., H. Zebker, P. Segall, and F. Amelung (2002), Fault slip distribution of the 1999 Mw 7.1 Hector Mine, California earthquake, estimated from satellite radar and GPS measurements, *Bull. Seismol. Soc. Am.*, *92*, 1377–1389, doi:10.1785/0120000922.

Lanari, R., O. Mora, M. Manunta, J. J. Mallorqui, P. Berardino, and E. Sansosti (2004), A small-baseline approach for investigating deformation on full-resolution differential SAR interferograms, *IEEE Trans. Geosci. Remote Sens.*, *42*, 1377–1386, doi:10.1109/TGRS.2004.828196.

Lockwood, J. P., R. I. Tilling, R. T. Holcomb, F. Klein, A. T. Okamura, and D. W. Peterson (1999), Magma migration and resupply during the 1974 summit eruptions of Kilauea Volcano, Hawaii, *U.S. Geol. Surv. Prof. Pap.*, *1613*.

Miklius, A., P. Cervelli, M. Sako, M. Lisowski, S. Owen, P. Segal, J. Foster, K. Kamibayashi, and B. Brooks (2005), Global positioning system measurements on the Island of Hawai'i: 1997 through 2004, *U.S. Geol. Surv. Open File Rep.*, *2005-1422*.

Mogi, K. (1958), Relation between eruptions of various volcanoes and the deformation of the ground surfaces around them, *Bull. Earthquake Res. Inst. Univ. Tokyo*, *36*, 99–134.

Montgomery-Brown, E. K., D. K. Sinnet, M. Poland, P. Segall, T. Orr, H. Zebker, and A. Miklius (2010), Geodetic evidence for en echelon dike emplacement and concurrent slow slip during the June 2007 intrusion and eruption at Kilauea volcano, Hawaii, *J. Geophys. Res.*, *115*, B07405, doi:10.1029/2009JB006658.

Myer, D., D. Sandwell, B. Brooks, J. Foster, and M. Shimada (2008), Inflation along Kilauea's Southwest Rift Zone in 2006, *J. Volcanol. Geotherm. Res.*, *177*, 418–424, doi:10.1016/j.jvolgeores.2008.06.006.

Okada, Y. (1985), Surface deformation due to shear and tensile faults in a half-space, *Bull. Seismol. Soc. Am.*, *75*, 1135–1154.

Owen, S., P. Segall, M. Lisowski, A. Miklius, M. Murray, M. Bevis, and J. Foster (2000), January 30, 1997 eruptive event on Kilauea Volcano, Hawaii, as monitored by continuous GPS, *Geophys. Res. Lett.*, *27*, 2757–2760, doi:10.1029/1999GL008454.

Pepe, A., and R. Lanari (2006), On the extension of the minimum cost flow algorithm for phase unwrapping of multitemporal differential SAR interferograms, *IEEE Trans. Geosci. Remote Sens.*, *44*, 2374–2383, doi:10.1109/TGRS.2006.873207.

Poland, M., A. J. Sutton, and T. M. Gerlach (2009), Magma degassing triggered by static decompression at Kilauea Volcano, Hawaii, *Geophys. Res. Lett.*, *36*, L16306, doi:10.1029/2009GL039214.

Poland, M., A. Miklius, A. J. Sutton, and C. R. Thornber (2012), A mantle-driven surge in magma supply to Kīlauea Volcano during 2003–2007, *Nat. Geosci.*, *5*, 295–300, doi:10.1038/ngeo1426.

Rivalta, E., and P. Segall (2008), Magma compressibility and the missing source for some dike intrusions, *Geophys. Res. Lett.*, *35*, L04306, doi:10.1029/2007GL032521.

Rosen, P. A., S. Henley, G. Peltzer, and M. Simons (2004), Updated repeat orbit interferometry package released, *Eos Trans. AGU*, *85*, 47, doi:10.1029/2004EO050004.

Ryan, M. (1987), Neutral buoyancy and the mechanical evolution of magmatic systems, in *Magmatic Processes: Physiochemical Principles*, edited by B. O. Mysen, *Spec. Publ. Geochem. Soc.*, *1*, 259–287.

Sandwell, D. T., D. Myer, R. Mellors, M. Shimada, B. Brooks, and J. Foster (2008), Accuracy and resolution of ALOS interferometry: Vector deformation maps of the Father's Day Intrusion at Kilauea, *IEEE Trans. Geosci. Remote Sens.*, *46*, 3524–3534, doi:10.1109/TGRS.2008.2000634.

Segall, P., P. Cervelli, S. Owen, M. Lisowski, and A. Miklius (2001), Constraints on dike propagation from continuous GPS measurements, *J. Geophys. Res.*, *106*(B9), 19,301–19,317, doi:10.1029/2001JB000229.

Stephen, M. L., Y. Sever, W. L. Bertiger, M. Heflin, K. Hurst, R. J. Muellerschoen, S. C. Wu, T. Yunk, and J. Zumberge (1996), *GIPSY-OASIS II: A High Precision GPS Data Processing System and General Satellite Orbit Analysis Tool*, Jet Propul. Lab., Calif. Inst. of Technol., Pasadena.

Swanson, D. A., T. R. Rose, R. S. Fiske, and J. P. McGeehin (2012), Keanakako'i Tephra produced by 300 years of explosive eruptions following collapse of Kīlauea's caldera in about 1500 CE, *J. Volcanol. Geotherm. Res.*, *215–216*, 8–25 doi:10.1016/j.jvolgeores.2011.11.009.

Tilling, R. I., and J. J. Dvorak (1993), Anatomy of a basaltic volcano, *Nature*, *363*, 125–133, doi:10.1038/363125a0.

Wallace, M. H., and P. T. Delaney (1995), Deformation of Kilauea volcano during 1982 and 1983: A transition period, *J. Geophys. Res.*, *100*(B5), 8201–8219, doi:10.1029/95JB00235.

Wilson, D., T. Elias, T. Orr, M. Patrick, J. Sutton, and D. Swanson (2008), Small explosion from new vent at Kilauea's summit, *Eos Trans. AGU*, *89*, 203, doi:10.1029/2008EO220003.

Wright, T. J., B. E. Parsons, and Z. Lu (2004), Toward mapping surface deformation in three dimensions using InSAR, *Geophys. Res. Lett.*, *31*, L01607, doi:10.1029/2003GL018827.

Yang, X., P. M. Davis, P. T. Delaney, and A. T. Okamura (1992), Geodetic analysis of dike intrusion and motion of the magma reservoir beneath the summit of Kilauea Volcano, Hawaii: 1970–1985, *J. Geophys. Res.*, *97*(B3), 3305–3324, doi:10.1029/91JB02842.